

Optical properties of an effective one-band Hubbard model for the cuprates

M. E. Simon, A. A. Aliaga and E. R. Gagliano
 Centro Atómico Bariloche and Instituto Balseiro
 Comisión Nacional de Energía Atómica
 8400 S.C. de Bariloche, Argentina.
 (Received March 23, 2024)

We study the Cu and O spectral density of states and the optical conductivity of CuO_2 planes using an effective generalized one-band Hubbard model derived from the extended three-band Hubbard model. We solve exactly a square cluster of 10 unit cells and average the results over all possible boundary conditions, what leads to smooth functions of frequency. Upon doping, the Fermi energy jumps to Zhang-Rice states which are connected to the rest of the valence band (in contrast to an isolated new band in the middle of the gap). The transfer of spectral weight depends on the parameters of the original three-band model not only through the one-band effective parameters but also through the relevant matrix elements. We discuss the evolution of the gap upon doping. The optical conductivity of the doped system shows a mid-infrared peak due to intraband transitions, a pseudogap and a high frequency part related to interband transitions. Its shape and integrated weight up to a given frequency (including the Drude weight) agree qualitatively with experiments in the cuprates for low to moderate doping levels, but significant deviations exist for doping $x > 0.3$.

PACS numbers: 74.72.-h, 78.20.-e, 79.60.-i, 75.40.Mg

I. INTRODUCTION

In recent years, there has been much interest in the spectral and related electronic properties of cuprates superconductors and similar materials [1,31]. In spite of the considerable research effort, there are several issues which remain to be clarified. For example, photoemission experiments at optimal doping [1] show that electrons have a large Fermi surface of area $(1-x)$ where x is the amount of hole doping, while at small doping it is expected that the Fermi surface consists of four small hole pockets centered at $(\pm 2; \pm 2)$ of total area x . The evolution of the Fermi surface remains a tough problem [31]. There is a recent theoretical study on this subject [32].

Another related issue is the appearance and evolution for $x \neq 0$ of states at energies which lie in the gap for $x = 0$. There are at least two physical pictures. On the basis of several measurements, and particularly the change of sign of the Hall constant with x in $\text{La}_{2-x}\text{Sr}_x\text{CuO}_4$, Sreedhar and Ganguly [2] proposed that the gap in the spectral density gradually closes with increasing x , and after the closing, the system has completed its evolution from a Mott (or better said "charge-transfer") insulator to a band metal. As soon as doping begins the Fermi level jumps to the valence band. This jump is consistent with the measured x-ray absorption spectrum (XAS) [6,7]. Instead, from the optical conductivity [3] and high-energy spectroscopies [5], it has been suggested that a new band of midgap states is formed, taking spectral weight from both, conduction and valence bands, and the Fermi level remains in the midgap band. A minimal shift of the Fermi level with doping has been observed by photoemission in $\text{La}_{2-x}\text{Sr}_x\text{CuO}_4$ [8] and in the electron doped $\text{Nd}_{2-x}\text{Ce}_x\text{CuO}_4$ [9], but

not in $\text{Ba}_2\text{Sr}_2\text{Ca}_{1-x}\text{Y}_x\text{CuO}_2\text{C}_8$ [10]. It might be possible that the states in the middle of the gap are created by deep donor levels originated by the substitution of La^{+3} by Sr^{+2} ions. The resulting "in-purity-state model" is consistent with the experimental evidence in the oxide $(\text{Nd,Sr})\text{CoO}_3$ [13]. The effect of this substitution has been discussed in Ref. [7]. However, inhomogeneities are usually not included in the theoretical treatments, and it seems necessary to generalize the Hubbard model to explain the electronic structure of some non-stoichiometric oxides [13,14].

To discuss the validity of the translationally invariant three-band Hubbard model [33] or effective models derived from it [19,20,34,36] in the description of the cuprates, it is necessary to know precisely the spectral properties of these models. One of the most used and effective ways to study these properties in two dimensions at zero temperature is the exact diagonalization of small clusters [17,19,22,24,29]. Among the different effective models, those similar to the $t-J$ one [22,24,29,34,36] have the smallest number of states per unit cell. However, like the spin-fermion (or Kondo-Hohenberg) model [19,20], their Hilbert space is too small to allow a description of both, valence and conduction bands. In contrast, the number of states per unit cell of the three-band model is so large that the largest exactly solved cluster contains only four unit-cells [17,18,23]. Thus, the most appropriate effective model to study the evolution of the gap seems to be the extended Hubbard one [35]. Numerical studies of the Hubbard model show a change of sign of the Hall constant as a function of doping, but it has not been related with a reconstruction of the spectral density [37,40]. The spectral properties of the Hubbard model have been calculated in periodic square clusters of 8, 10 and 16 sites [21,23]. Without artificial broadening,

the result of these calculations is given by a set of delta functions at different frequencies (see for example Fig. 11 of Ref. [22]), from which it is not possible to distinguish if in the thermodynamic limit there is one, two or more gaps in the spectral density of states. Also the Druđe weight shows significant size effects, being negative near half-filling.

In this work we solve exactly the effective one-band extended Hubbard Hamiltonian in a square cluster of 10 unit cells and average over all possible boundary conditions [41]. This technique has been also used by Poilblanc to study the optical conductivity of the t - J model [24] and by Xiang and Wheatly [42] to calculate the dispersion relation of one hole in a generalized t - J model, obtaining good agreement with results of the self-consistent Born approximation and experiments in $\text{Sr}_2\text{CuO}_2\text{Cl}_2$. To our knowledge this approach has not been applied to the spectral properties of Hubbard or extended Hubbard clusters. It allows us to obtain continuous spectral densities and optical conductivities and according to our studies in small rings (see section III), the convergence to the thermodynamic limit is faster.

It must also be pointed out that the spectral properties of the Hubbard model derived from the numerical methods mentioned above, as well as analytical studies of the change in the spectral weights with doping [30] do not directly correspond to the cuprates as described by the original three-band Hubbard model. To calculate any property of this model using an effective Hamiltonian, one should transform the corresponding operators from the three-band to the effective Hamiltonian. This has been done for the spin-fermion [19], Hubbard [44] and t - t' - J [36] as effective models for the cuprates. In particular, Feiner explained the electron-hole asymmetry in the spectral weight in the cuprates (which is absent in the "isolated" Hubbard model) [44]. Here we use and discuss the transformed operators for spectral density and optical conductivity.

In section II, we briefly review the extended one-band Hubbard model as an effective model for cuprate superconductors, and construct the relevant operators. In section III, we discuss the numerical techniques and the method of integrating over arbitrary boundary conditions. In section IV, we present the results for the spectral density, while section V contains the results for the optical conductivity, Druđe weight and related quantities. The conclusions are presented in Section VI.

II. THE EFFECTIVE EXTENDED ONE-BAND HUBBARD MODEL AND TRANSFORMED OPERATORS

Experimental evidence about the symmetry of holes in high- T_c superconductors [5,45,46], as well as constrained-density-functional calculations [47,48], support the ap-

propriateness of the three-band Hubbard model [33] for the description of these systems. The Hamiltonian is:

$$H_{3b} = \sum_j \sum_j' t_{jj'}^y p_j^\dagger p_{j'} + t_{pd} \sum_i (p_{i+}^\dagger d_i + h.c.) \quad (1)$$

$$+ \sum_j t_{pp} p_{j+}^\dagger p_j + U_{pd} \sum_i n_i^d n_{i+}^p + U_d \sum_i n_i^d n_{i\#}^d + U_p \sum_j n_j^p n_{j\#}^p$$

where d_i^\dagger (p_j^\dagger) creates a hole in the $d_{x^2-y^2}$ (p) orbital at site i (j) with spin \uparrow , $i+$ ($j+$) label the four O atoms nearest-neighbors to Cu (O) site i (j). The phases of half the d and p orbitals have been modified by a factor (-1) in order to have $t_{pd} > 0$ and $t_{pp} > 0$ independently of the direction. While other Cu and O orbitals should be included to explain Raman experiments [49,50], these additional states affect neither low-energy spectral properties (below the bottom of the p band [50]) nor the validity of the one-band effective model H_{1b} [50].

The transformation of the low-energy part of H_{3b} to the effective model H_{1b} can be summarized in four steps [34,35,50,51]: (i) change of basis of the O orbitals $p_j^x; p_j^y$ to orthogonal Wannier functions $w_i; w_{i'}$ centered at each Cu site i , with symmetries b_{1g} (the same as the $d_{x^2-y^2}$ orbital) and a_{1g} respectively; (ii) exact solution of the cell Hamiltonian H_i (the terms of H_{3b} which contain only operators acting on cell i); (iii) mapping the low-energy states $|j\rangle$ of H_{3b} into corresponding ones $|j\rangle$ of the Hilbert space of the one band model ($|j\rangle \equiv |j\rangle$); (iv) transform the operators H_i and H_{3b} to the new basis $|j\rangle$. A transformed operator O can be expressed in terms of the matrix elements of the original operator O as:

$$O = \sum_{n,m} \langle n | O | m \rangle |n\rangle \langle m| \quad (2)$$

Finally, the effect of states of H_{3b} which do not have corresponding ones in H_{1b} can be included as perturbative corrections [35], but we will not do it here. In Fourier space, the p orbitals are related with the O Wannier functions by:

$$p_k^x = \frac{1}{2} \left(\cos\left(\frac{k_x a}{2}\right) w_k + \cos\left(\frac{k_y a}{2}\right) w_{k'} \right) \quad (3)$$

$$p_k^y = \frac{1}{2} \left(\cos\left(\frac{k_y a}{2}\right) w_k + \cos\left(\frac{k_x a}{2}\right) w_{k'} \right)$$

with $w_k = \left(1 + \frac{1}{2} \cos(k_x a) + \frac{1}{2} \cos(k_y a)\right)^{\frac{1}{2}}$. The eigenstates of H_i retained in the mapping procedure are (in addition to the vacuum at site i), the lowest one-hole doublet $|j\rangle$ and the lowest two-hole doublet $|j_2\rangle$. They can be expressed as:

$$|j_2\rangle = \frac{A_1}{\sqrt{2}} (c_{i\#}^y c_{i\#}^y - c_{i\#}^y c_{i\#}^y) |j_1\rangle \quad (4) \quad \text{where}$$

$$|j_1\rangle = B_1 c_i^y - B_2 c_i^y |j_1\rangle$$

These states are mapped into those of the one-band model by the correspondence $|j_1\rangle \rightarrow c_i^y |j_1\rangle$, $|j_2\rangle \rightarrow c_{i\#}^y c_{i\#}^y |j_1\rangle$. This assignment and Eq.(2) applied to H_{3b} leads to the effective one-band generalized Hubbard Hamiltonian [35], with occupation dependent nearest-neighbor hopping and repulsion (interactions and hoppings at larger distances are neglected for simplicity):

$$H_{1b} = E_1 \sum_i n_i + U \sum_i n_i n_{i\#} + \sum_{\langle ij \rangle} c_j^y c_i^\dagger t_{AA} (1 - n_i) (1 - n_j) + t_{AB} [n_i (1 - n_j) + n_j (1 - n_i)] + t_{BB} n_i n_j + g + h.c. + \sum_{\langle ij \rangle} f V_{11} (1 - n_i) (1 - n_j) + V_{22} n_i n_j + V_{12} [(1 - n_i) n_j + n_i (1 - n_j)] n_i n_j \quad (5)$$

Several particular cases of this model have been widely studied [52-58]. For $t_{AA} + t_{BB} = 2t_{AB}$ and $V_{ij} = 0$, the model is shown to lead to superconductivity for small U and adequate doping [52], particularly in one dimension [53-55]. For $V_{ij} = t_{AB} = 0$, the model has been exactly solved in one dimension [56]. For $t_{AB} = 0$, $V_{22} = V_{21} = V_{11}$ and half-filling, the exact ground state has been found in a wide range of parameters for arbitrary lattices in arbitrary dimension, and the phase diagram separating metallic, Mott insulating and charge-density waves regions has been established [57].

The spectral properties in two dimensions have been studied numerically in the charge-density-wave (large V_{ij}) regime [58], and for $V_{ij} = 0$ and small t_{AB} at half-filling [59]. The model has been also used recently to study the regions of phase separation and valence instabilities of the original three-band model [35]. Typical values of the parameters of H_{3b} and H_{1b} are given in tables I and II respectively.

At zero temperature, the Cu and O spectral densities are defined by:

$$\rho_o(\omega) = \frac{1}{L} \sum_{k,m} \langle j_1 | \mathcal{O}_k | j_1 \rangle^2 \delta(\omega + E_g - E_n) \quad (6)$$

where $|j_1\rangle, E_n$ are the eigenstates and energies of H_{1b} , $|j_1\rangle$ labels the ground state for a given number of particles N and L is the number of unit cells in the system. For electron spectral densities of Cu or one of both O atoms in the unit cell (measured by inverse photoemission), \mathcal{O}_k is the operator in the representation of H_{1b} of d_k or $p_k^{x,y}$ respectively. For hole spectral densities (corresponding to photoemission) the corresponding hermitian conjugate operators should be taken. In real space using Eq.(2) one obtains:

$$d_i = D_1 c_i (1 - n_i) + D_2 c_i n_i \quad (7)$$

$$p_i = P_1 c_i (1 - n_i) + P_2 c_i n_i$$

$$D_1 = \hbar \omega |j_1\rangle \langle j_1| = B_1 \quad (8)$$

$$D_2 = \hbar \omega |j_2\rangle \langle j_2| = \left(\frac{A_1 B_2}{2} + A_3 B_1 \right)$$

$$P_1 = \hbar \omega |j_1\rangle \langle j_1| = B_2$$

$$P_2 = \hbar \omega |j_2\rangle \langle j_2| = \left(\frac{A_1 B_1}{2} + A_2 B_2 \right)$$

Transforming Fourier and using Eq.(3), the operators entering Eq.(6) are defined. As will be discussed in section IV, the asymmetry of Eq.(7) and also the Hamiltonian Eq.(5) under electron-hole transformation leads to a different behavior of the spectral densities under electron or hole doping. This difference is apparent in the cuprates and in the three-band Hubbard model results, but it is absent in the ordinary one-band Hubbard model [18,44].

The optical conductivity can be written as [16,17]

$$\sigma(\omega) = 2 \text{Im} \chi(\omega) + \text{reg}(\omega) \quad (9)$$

where

$$\text{reg}(\omega) = \frac{1}{V} \sum_{n \notin g} \langle j_1 | j_k j_l | j_1 \rangle^2 \delta(E_n - E_g - \omega) \quad (10)$$

V is the volume of the system, j_k the x component of the current operator. The Drued weight D can be calculated in two ways: either using the mean value of the kinetic energy in a given direction $\hbar T_{xi}$:

$$D = \left(\frac{ea}{\hbar} \right)^2 \frac{\hbar T_{xi}}{2V} \frac{1}{V} \sum_{n \notin g} \frac{\langle j_1 | j_k j_l | j_1 \rangle^2}{E_n - E_g} \quad (11)$$

or from the second derivative of the energy with respect to the vector potential A in a system with periodic (or arbitrary as described in the next section) boundary conditions

$$D = \frac{c^2}{2V} \frac{d^2 E(A)}{dA^2} \Big|_{A=0} \quad (12)$$

The current operator can be derived in a standard way, from $dH = dA$, when each hopping term $c_i^y c_j$ is multiplied by a phase factor $\text{Exp}[ieA(x_i - x_j)] = (\tilde{c})$ [16,17]. In the case of the effective Hamiltonian Eq.(5), the current

can be divided in three terms proportional to the three different types of hopping terms:

$$\mathbf{j}_k = \mathbf{j}_{AA} + \mathbf{j}_{AB} + \mathbf{j}_{BB} \quad (13)$$

with

$$\mathbf{j}_{AA}(r) = \frac{iae}{\sim} t_{AA}^X (c_r^y c_{r+x} - c_{r+x}^y c_r) (1 - n_r;) (1 - n_{r+x};) \quad (14)$$

$$\mathbf{j}_{AB}(r) = \frac{iae}{\sim} t_{AB}^X (c_r^y c_{r+x} - c_{r+x}^y c_r) [(1 - n_r;) n_{r+x}; + n_r; (1 - n_{r+x};)]$$

$$\mathbf{j}_{BB}(r) = \frac{iae}{\sim} t_{BB}^X (c_r^y c_{r+x} - c_{r+x}^y c_r) n_r; n_{r+x};$$

An alternative derivation of the current operator for the effective one-band model is to obtain first the current operator of the multiband model [17], then project the result into the low-energy subspace and map it onto the one-band representation. Both derivations lead to identical results if $t_{pp} = 0$. For realistic values of t_{pp} , there are small differences between the resulting coefficients entering the current \mathbf{j}_{AA} ; \mathbf{j}_{AB} and \mathbf{j}_{BB} . For example while for the set 2 of parameters of H_{3b} (see table I) we obtain $t_{AA} = t_{AB} = 0.38$, $t_{BB} = 0.33$, in the second derivation these values should be replaced by -0.32 , -0.35 and -0.36 in the respective currents. This difference is probably due to the different way in which excited (mainly local triplet) states are taken into account in lowest order in both procedures when $t_{pp} \neq 0$ [60,36]. In this work we use Eq.(14).

III. NUMERICAL METHODS AND AVERAGE OVER BOUNDARY CONDITIONS

We have evaluated Eqs.(6), (10) and (11) using the now standard continued-fraction expansion of these equations with the Lanczos method [62], in a square cluster of 10 unit cells, integrating the result over the different boundary conditions [41,24]. Particular boundary conditions are specified by two phases $(i; j)$, $0 \leq i < 2$ in the following way: an infinite square lattice is divided into square 10-site clusters, and the sites which are at distances $nV_1 + mV_2$ with $n; m$ integers and $V_1 = (3;1)$; $V_2 = (1;3)$ are considered equivalent (see Fig.1). After choosing a particular 10-site cluster, each "time" the hopping term makes a particular jump out of the cluster, it is mapped back into the cluster through a translation in one of the vectors $V_1; V_1; V_2$; or V_2 and the wave function is multiplied by e^{i_1} ; e^{-i_1} ; e^{i_2} or e^{-i_2} respectively. When $(i; j) = (0;0)$ this is equivalent to the usual periodic boundary conditions. It is easy to see that when we impose the wave function for N particles to be an irreducible representation of the group of translations of the

infinite square lattice, the allowed total wave vectors K should satisfy

$$\begin{aligned} N_{i_1} + 2n_1 &= K_x \quad V_1 \\ N_{i_2} + 2n_2 &= K_y \quad V_2 \end{aligned} \quad (15)$$

where $n_1; n_2$ are integers. Solving for $K_x; K_y$ one obtains:

$$\begin{aligned} K_x &= \frac{N}{10} (3 - i_1 - i_2) + \frac{2(n_2 - 3n_1)}{10} \\ K_y &= \frac{N}{10} (1 + 3 - i_2) + \frac{2(3n_2 + n_1)}{10} \end{aligned} \quad (16)$$

When $(i; j) = (0;0)$, varying the integers $n_1; n_2$, Eqs.(16) give the 10 inequivalent wave vectors allowed by periodic boundary conditions. When $(i; j)$ is allowed to vary continuously the whole reciprocal space can be swept. This allows us to obtain more information from the finite-size cluster calculations. Also, while the spectral densities and optical conductivities being calculated are given by a sum of delta functions for each $(i; j)$ (Eqs.(6) and (9)), integrating the result over $(i; j)$ leads to continuous functions. In practice we have replaced the integral by an average over a square mesh of up to 8×8 points (up to 34 non-equivalent by symmetry for the optical conductivity) in $(i; j)$ space until a fairly smooth function was obtained.

However, the procedure described above has some shortcomings when applied to the optical conductivity. For general boundary conditions there is a spontaneous current in the ground state, invalidating the derivation of Eqs.(9) to (12) [16,17]. (Such a current can not exist in the thermodynamic limit, even if it were allowed by symmetry [63,64]). In finite systems, this current is zero for periodic boundary conditions at "closed-shell" fillings, (including half-filling in our cluster), and for half-filling and any boundary conditions in the $U \rightarrow 1$ limit (as in the $t - J$ model [24]), since in this limit the charge dynamics is suppressed. Our point of view is that the average of Eqs.(10) and (11) over boundary conditions in a finite system, is an approximation to the correct expression in the thermodynamic limit, which converges faster with system size than the result of Eqs.(10) and (11) or (12) for fixed boundary conditions. Since we have not done finite-size scaling in two dimensions, we

can not prove this statement. However, it is supported by our one-dimensional check summarized below. Furthermore, as we shall see in section V, the results using the averaging procedure look reasonable, while the Drued weight obtained in larger systems using periodic boundary conditions show unphysical negative values at half-filling [22,27]. Previous calculations of the optical conductivity of the t - J model using twisted boundary conditions also support our procedure [24].

We have checked the method of averaging over boundary conditions applying it to the optical conductivity ($\sigma(\omega)$) of one-dimensional Hubbard rings, for which finite-size scaling can be done, and some exact results, like the charge gap, are available [43]. The results for $U=t=4;6$ and 8 and several system sizes L are represented in Figs.2-4 respectively. A funny feature of these curves is the presence of oscillations in $\sigma(\omega)$. A comparison of the result for rings of different sizes shows that this is a finite-size effect. Calculations using spin-wave theory in the strong coupling limit give a smooth $\sigma(\omega)$ [26]. Fortunately no signs of these oscillations are present in the two-dimensional case. By comparison, the strong coupling limit of the Hubbard model, and the t - J model with one hole in systems as large as 19 sites with periodic boundary conditions shows a few delta functions [26].

The presence of a peak at zero frequency is a consequence of the already discussed spontaneous current in the ground state for general boundary conditions. Clearly, this is also a finite-size effect and the height of the peak decreases with system size and also with increasing $U=t$. Thus, we have suppressed this peak in the two-dimensional results of section V.

We have also noticed that the gap in $\sigma(\omega)$ converges much faster to the thermodynamic limit E_g than the corresponding result using fixed boundary conditions. In table III, we compare the exact gap, given by the integral [43];

$$\frac{E_g}{t} = \frac{16t}{U} \int_0^1 \frac{dy}{\sinh(\frac{2-y}{U})} \quad (17)$$

against its value (taken as the position of the lowest frequency peak in the spectra of Figs. 2-4) for a ring of 8 sites after averaging over boundary conditions and at fixed antiperiodic boundary condition. Clearly, the averaging procedure speeds up the convergence toward the $L \rightarrow \infty$ limit.

IV. THE SPECTRAL DENSITIES

In Fig.5, we show the Cu and O spectral densities ($\rho(\omega)$) in the hole representation (photoemission and inverse photoemission correspond to $\omega > E_F$ and $\omega < E_F$ respectively, where E_F is the Fermi energy) for several doping levels and the set of parameters 1 (see Tables I and II

). These spectral densities have been calculated as described in section III, using Eq.(6) with O_k replaced by c_k^y, p_k^{xy} for Cu and O photoemission, and by d_k, p_k^x for inverse photoemission. The result for O has been multiplied by a factor 2 to represent the total contribution of both 2p orbitals of the unit cell. Also shown in Fig.5 are the extended Hubbard spectral densities corresponding to the operators $c_k^y (\omega > E_F)$ and $c_k (\omega < E_F)$. Note that in contrast to the usual Hubbard model, the extended Hubbard spectral densities are not symmetric under hole ($x > 0$) or electron ($x < 0$) doping. This is due mainly to the fact that $t_{AA} \neq t_{BB}$. However, the asymmetry of the Cu and O spectral densities is much stronger. In agreement with experiment, for hole doping, the inverse photoemission spectrum near E_F shows a larger contribution of O states than Cu d states, while for electron doping, the photoemission spectrum near the Fermi level is dominated by Cu states.

A pseudogap in the spectral densities persists with doping and allows to separate the electronic states in two bands at lower and higher energies than this pseudogap. The lower band corresponds to states with low double occupancy and therefore, the spectral densities are dominated by the contribution proportional to $c_i (1 - n_i)$ in Eq.(7); thus the Cu and O spectral densities in the lower band are, as a first approximation proportional to the respective coefficients (B_1 and B_2 , see Eq.(8)) in the one-particle ground state of the cell. However, the states of the lower band contain some admixture of double occupied states, and this introduces an energy dependence of the relative weight of Cu and O states. The states of lower energy ($\omega < 1$) have a larger Cu content than those of the rest of the lower band. Similarly, as discussed previously by Feiner [44], the Cu and O contents of the upper band are mainly determined by D_2 and P_2 respectively (see Eq.(8)), which depend on the structure of the Zhang-Rice singlet $|\psi_i\rangle$ and the ground state of the cell with one hole $|\psi_i\rangle$ (see Eq.(4)).

From Eq.(6) applied to the Hubbard operators c_k and c_k^y , it is easy to obtain the total inverse photoemission N^- and photoemission N^+ spectral weight:

$$N^- = \int_{E_F}^{\infty} \rho_c(\omega) d\omega = \langle n_{i\uparrow} \rangle + \langle n_{i\downarrow} \rangle = 1 + x \quad (18)$$

$$N^+ = \int_{-\infty}^{E_F} \rho_{c^+}(\omega) d\omega = 2 \langle n_{i\uparrow} \rangle - \langle n_{i\downarrow} \rangle = 1 - x$$

These sum rules are the same as those corresponding to the usual Hubbard model. However, using Eqs.(6) and (7) the following sum rules for the Cu orbital $d_x^2 - y^2$ and "antibonding" O Wannier function are obtained:

$$N_d^- = n_{d\uparrow} + n_{d\downarrow} = (1+x)D_1^2 + 2d(D_2^2 - D_1^2) \quad (19)$$

$$N_d^+ = 2(d-x)D_1^2 + (1+x-2d)D_2^2$$

$$N_p^- = n_{p\uparrow} + n_{p\downarrow} = (1+x)P_1^2 + 2d(P_2^2 - P_1^2)$$

$$N_p^+ = 2(d-x)P_1^2 + (1+x-2d)P_2^2$$

where $d = \langle n_i n_{i\#} \rangle$. Adding the four functions, the total spectral weight becomes:

$$N_t = (1+x)(1 + D_2^2 + P_2^2) - 2x \quad (20)$$

Since $D_2^2 + P_2^2 < 1$, then $N_t < 2$. The rest of the spectral weight has been projected out of the low-energy effective extended Hubbard model and it is contained at higher energies. The spectral weights given by Eqs.(19) as a function of doping are represented in Fig.6 for a typical set of parameters of the three-band model. In Fig.7, we show the coefficients P_i, D_i of the effective operators (Eq.(8)) as a function of the three-band model parameter x . We also show the function $[1 - (D_2^2 + P_2^2)]$, related by Eq.(20) to the amount of spectral weight projected out of the effective low-energy Hamiltonian. From the slopes of N_d and N_p as a function of doping (Fig.6) one realizes that when doping the stoichiometric compound with electrons, the latter occupy mainly Cu states, while for hole doping, holes occupy mainly O states, and for the parameters of Fig.6, part of the Cu holes are transferred to O holes. This is a well known effect of the Cu-O repulsion U_{pd} [35].

From the above discussion, it is clear that the main features (peaks and valleys) of the Cu and O spectral densities are present in the corresponding extended Hubbard result (obtained with the c_x and c_x^y operators), and as a first approximation, the former can be obtained from the latter modifying the spectral weights of the lower and upper Hubbard bands with the coefficients given by Eqs.(8) and represented in Fig.7. Thus in the following we discuss the general properties of the extended Hubbard spectral density (independently of the mapping procedure) and the spectral weight of both extended Hubbard bands.

In Fig.8 we show the evolution with hole doping of the spectral density of states of the extended Hubbard model. As discussed previously in the case of the ordinary Hubbard model [22], after doping, states appear in the gap of the stoichiometric compound and the Fermi level jumps to the upper Hubbard band. According to our results, these states are distributed evenly inside the gap and there is not an impurity band at a defined energy. Also, the pseudogap persists for all dopings, and both bands evolve smoothly with doping, with a noticeable transfer of spectral weight from the lower to the upper band. In Fig.9, we show the same results for the set of parameters 3 of Tables I and II, for which the ratio of the on-site Coulomb repulsion to hopping parameters is larger. In this case, the weight of the states which appear in the gap after doping is much smaller, and also the amount of spectral weight transfer between the bands is smaller. Note also and by contrast to the usual Hubbard model the strong asymmetry of $(!)$ at $x = 0$ due to $t_{AA} \ll t_{BB}$.

The transfer of spectral weight in the Hubbard model has been discussed previously [7,30] and is important in the analysis of x-ray absorption spectra in the cuprates

[6,7]. In the strong-coupling limit (large U), or in the Hubbard III approximation, a static spectral weight of $2x$ is easily obtained ($1-x$ states lie in the upper Hubbard band). However, as the hopping increases, a positive dynamical contribution to the spectral weight becomes important. In Fig.10 we show this dynamical contribution for the extended Hubbard model and the three sets of parameters of Table II. It is apparent that for realistic parameters for the cuprates, the dynamical contribution is very important, and as could be seen comparing Figs. 8 and 9, it is more important for smaller ratios $U=t_m$, where $t_m = (t_{AA} + 2t_{AB} + t_{BB})/4$ is the average effective hopping.

V. THE OPTICAL CONDUCTIVITY

For the evaluation of Eqs.(10) and (11), we have taken the distance between planes $d_z = 6.64 \text{ \AA}$, corresponding to La_2CuO_4 . Thus, the Drude weight D and the regular part of the optical conductivity $\sigma_{reg}(!)$ are proportional to the constant $2e^2/(\sim d_z) = 3.7 \cdot 10^3 \text{ cm}^{-1}$. The resulting Drude weight and average value of the kinetic energy as a function of hole doping are represented in Fig.11 for the choice of parameters 3 of Table II. The corresponding results for the optical conductivity are shown in Fig.12. The average over all boundary conditions has been replaced by a discrete sum over a square mesh of 8×8 points $(i; j)$ (34 non-equivalent by symmetry). For more than 16 points the results are practically independent on the number of different boundary conditions taken.

For the semiconducting system ($x = 0$), there is a spurious peak at $! = 0.4$. This is a finite-size effect related with the fact discussed in section III, that the ground state for general boundary conditions carry a current for finite U . The peak corresponds to transitions to excited states which differ from the ground state mainly in the spin arrangement. For realistic and large U the magnitude of the spurious peak is small. In Fig.13, we show the optical conductivity for a smaller value of the effective U after averaging over $32 (i; j)$ points (18 non-equivalent by symmetry). The magnitude of the spurious peak increases, but all the other features are very similar between them, and qualitatively similar to previous results obtained in periodic 4×4 clusters [21]. However, our procedure of averaging (Eq.(11)) over boundary conditions leads to more reasonable (small and positive) values of the Drude weight for the insulating system: $5 \cdot 10^5$ and $3 \cdot 10^3 \text{ cm}^{-1}$ for the set 3 and 2 of parameters respectively.

For $x = 0.2$, the results are in semiquantitative agreement with experiments [3,4]. Excluding the spurious peak near 0.4, the optical conductivity of the insulating compound shows a gap of $\sim 2\text{eV}$ and a characteristic shape at larger energies. Moreover, if the scale

of energies is modified by a $t_{AB}=4$, the main features of Fig.13 for $x = 0$ coincide with the observed spectral dependence of the persistent photoconductivity in $YBa_2Cu_3O_{6.38}$ [12]. As the system is doped the spectral intensity above $2eV$ decreases and at the same time, a mid-infrared peak appears. Although this low-frequency peak has been discussed before, its nature has not been clarified yet. Recently, an explanation based on the string picture of the t_{AB} model has been proposed [29]. In order to shed light on the origin of the different contributions to the optical conductivity, we have separated the contributions of the three currents, j_{AA} ; j_{BB} and j_{AB} , and compared them with the spectral density, as shown in Fig.14. For hole-doped systems, the contribution of j_{AA} is negligible. From the analysis of Fig.14, we conclude that the optical conductivity at energies of the order of the gap and above corresponds to transitions between the lower and upper extended Hubbard bands, originated by t_{AB} (which corresponds to a hopping between two nearest-neighbor singly-occupied sites). Instead, the mid-infrared peak corresponds to one-particle excitations inside the upper Hubbard band (from below to above the Fermi level), originated by t_{BB} or in other words (in agreement with Ref. [29]) to movements of the added holes without changing the amount of doubly occupied sites. The difference between the total optical conductivity and the contributions of j_{AA} and j_{BB} represented in Fig.14 is mainly due to cross terms involving both currents.

In Fig.15 we show the frequency dependent effective number of carriers defined by

$$N_{\text{ef}}(\omega) = \frac{2m_0V}{e^2N_0} \sum_{l=0}^Z |\langle l^0 | d | l^0 \rangle| \quad (21)$$

for the two sets of parameter used before in this section. In order to compare with experiment, we took the lattice parameter of the CuO_2 planes $a = 3.78\text{\AA}$, which corresponds to La_2CuO_4 . As well as the results shown in Figs. 12 and 13, the agreement with experiment is good for $x = 0.2$. Experimentally, for $x = 0.3$ there seems to be an abrupt change of regime to an uncorrelated metal, with the Drude peak as the only significant feature of the optical conductivity. Instead, our results do not show such a transition, but only a smooth evolution. Possible reasons of this discrepancy are discussed in the next section.

VI. SUMMARY AND DISCUSSION

Using an effective extended Hubbard model for the cuprates, we have calculated the Cu and O spectral density and optical conductivity in a square cluster of 10 unit cells, averaging over all possible boundary conditions. To our knowledge, this is the largest cluster for

which Cu and O spectral densities are calculated using the Lanczos method. The averaging procedure allows to obtain continuous spectral densities and optical conductivity, and leads to more reasonable values of the Drude weight near stoichiometry.

We obtain that the states which appear in the gap after doping are distributed evenly inside it, without building a new band of midgap or impurity like states. We also obtain that a marked pseudogap persists for all dopings, separating two bands. When the insulator is doped, the Fermi level jumps into the band which corresponds according to the sign of the doping. As doping proceeds, spectral weight is transferred to the band which contains the Fermi level from the other one. An analysis of the different components of the current operator allows us to conclude that the mid-infrared peak in the optical conductivity observed in doped systems is related to intra-band transitions across the Fermi level. The shape of the Cu and O spectral densities is consistent with the fact that for hole doping, holes enter mainly O p states, while Cu states are occupied on electron doping.

In general, these results are in agreement with experiment. There is however a disagreement with some optical experiments [8,9] which indicated almost no shift of the Fermi level with doping, as mentioned in section I. We should mention that, as discussed by Hybertsen et al. [7] the substitution of La^{+3} by Sr^{+2} creates a potential which might localize the doped holes by small doping, creating an impurity band of acceptor levels like in ordinary semiconductors. To include these effects it would be necessary to generalize the three-band Hubbard model and the effective models derived from it.

We do not obtain a deep reconstruction of the electronic structure around hole doping for $x = 0.3$ as conductivity [3], Hall and other experiments [2] suggest. A closing of the Mott-Hubbard gap was expected for similar dopings [2]. This closing in fact can occur in the three-band Hubbard model and the effective extended one band model for $U_{pd} = 3-4$. For these large values of U_{pd} the effective U of the one band model decreases with doping and a large transfer of holes from Cu to O takes place [35]. However, these values of U_{pd} are too large compared to the most accepted ones. For realistic parameters of the three-band model, the effective model parameters are independent of doping [35]. This does not exclude the possibility that the three-band parameters change near $x = 0.3$, as a consequence of screening caused by the added holes, for example. Nevertheless, the fact that there are always two bands as a function of doping is in agreement with x-ray absorption experiments in $La_{2-x}Sr_xCuO_4$ [6,7].

Due to the small size of the cluster, we have looked neither for the presence of a Kondo-like peak near the Fermi energy [15], nor the effects of excitons in the optical conductivity, which are present in the effective model for realistic and large V_{ij} [50]. A signal of the presence

- [38] B.S. Shastri, B.I. Shraiman, and R.R.P. Singh, Phys. Rev. Lett. 70, 2004 (1993).
- [39] A. Roj, G. Kotliar and G. Canright, Phys. Rev. B 47, 9140 (1993).
- [40] F.F. Assaad and M. Imada, Phys. Rev. Lett. 74, 3868 (1995).
- [41] C.G. Ross, Z Phys. B 86, 359 (1992).
- [42] T. Xiang and J.M. Wheatly, Phys. Rev. B 54, 12653 (1996).
- [43] A.A. Ovchinnikov, Soviet Phys. JETP 30, 1160 (1970) and references therein.
- [44] L. Feiner, Phys. Rev. B 48, 16857 (1993).
- [45] M. Takigawa, P.C. Hammel, R.H. Heener, Z. Fisk, K.C. Ott, and J.D. Thompson, Phys. Rev. Lett. 63, 1865 (1989).
- [46] J. Tranquada, S. Heald, A.M. Oodenaugh, and M. Suenaga, Phys. Rev. B 35, 7187 (1987); A. Fujimori, E. Takayama-Muromachi, Y. Uchida, and B. Okai, Phys. Rev. B 35, 8814 (1987); E. Pellegrin, N. Nucker, J. Fink, S.L.M. Oldtsov, A. Gutierrez, E. Navas, O. Strebel, Z. Hu, M. Domke, G. Kaindl, S. Ushida, Y. Nakamura, J. Mankl, M. Klauda, G. Saemann-Ischenko, A. Krol, J.L. Peng, Z.Y. Li, and R.L. Greene, Phys. Rev. B 47, 3354 (1993).
- [47] J.F. Annett, R.M. Martin, A.K. McManahan, and S. Sarpathy, Phys. Rev. B 40, 2620 (1989); J.B. Grant and A.K. McManahan, Phys. Rev. Lett. 66, 488 (1991).
- [48] M.S. Hybertsen, E.B. Stechel, M. Schluter and D.R. Jennison, Phys. Rev. B 41, 11068 (1990).
- [49] R. Liu, D. Salamon, M. Klein, S. Cooper, W. Lee, S-W Cheong, and D. Ginsberg, Phys. Rev. Lett. 71, 3709 (1993); D. Salamon, R. Liu, M. Klein, M. Karlow, S. Cooper, S-W Cheong, W. Lee, and D. Ginsberg, Phys. Rev. B 51, 6617 (1995).
- [50] M.E. Simon, A.A. Aligia, C.D. Batista, E.R. Gagliano, and F. Lema, Phys. Rev. B 54, R3780 (1996).
- [51] H.B. Schuttler and A.J. Fedro, Phys. Rev. B 45, 7588 (1992).
- [52] J. Hirsch, Physica C 158, 326 (1989); Phys. Lett. A 134, 351 (1989); F. Marsiglio and J. Hirsch, Phys. Rev. B 41, 6435 (1990).
- [53] Japaridze and E. Muller-Hartmann, Ann. Phys. (Leipzig) 3, 163 (1994).
- [54] L. Arrachea, A.A. Aligia, E.R. Gagliano, K. Hallberg, and C.A. Balseiro, Phys. Rev. B 50, 16044 (1994).
- [55] K. Michelsen and H. De Raedt, Int. J. Mod. Phys. to be published.
- [56] L. Arrachea, A.A. Aligia, and E.R. Gagliano, Phys. Rev. Lett. 76, 4396 (1996); references therein.
- [57] A.A. Aligia, L. Arrachea, and E.R. Gagliano, Phys. Rev. B 51, 13774 (1995); references therein.
- [58] Y. Otha, T. Tsuchi, W. Koshiba, and S. Maki, Phys. Rev. B 50, 13594 (1994).
- [59] E.R. Gagliano, A.A. Aligia, L. Arrachea, and M. Avignon, Phys. Rev. B 51, 14012 (1995).
- [60] M.E. Simon and A.A. Aligia, Phys. Rev. B 52, 7701 (1995).
- [61] A.A. Aligia, M.E. Simon and C.D. Batista, Phys. Rev. B 49, 13061 (1994).
- [62] E. Gagliano and C. Balseiro, Phys. Rev. Lett. 59, 2999 (1987).
- [63] E.I. Bunt, Phys. Rev. B 38, 6711 (1988).
- [64] M.E. Simon and A.A. Aligia, Phys. Rev. B 46, 3676 (1992).

FIGURE 1:
Scheme of the supercell (cluster) containing 10 unit cells used in our calculations. The vectors V_1 and V_2 generate the whole lattice by successive translations of the supercell.

FIGURE 2:
Average optical conductivity as a function of frequency for Hubbard rings of different length and $U=t=4$.

FIGURE 3:
Same as Fig.2, for $U=t=6$.

FIGURE 4:
Same as Fig.2, for $U=t=8$.

FIGURE 5:
Inverse photoemission ($! < E_F$) and photoemission ($! > E_F$) hole spectral densities for Cu (dashed line), O (full line) and Hubbard operator (dotted-dash line), for different hole dopings x . The vertical line indicates the position of the Fermi level E_F . Parameters are given by the set 1 of table I. The average over boundary conditions have been replaced by a discrete sum over 4×4 ($1; 2$) points (6 independent points).

FIGURE 6:
Total photoemission (N^+) and inverse photoemission (N^-) spectral weight for Cu (N_d) and O (N_p) as a function of hole doping. Parameters are $U_d = 9, t = 3, J_{pd} = 1, t_{pp} = 0.5, J_p = 4$.

FIGURE 7:
Parameters which define the effective low-energy Cu and O operators according to Eq.(8) as a function of x . Also shown is $1 - D_2^2 - P_2^2$, which is related with the high-energy spectral weight projected out of the low-energy effective Hamiltonian (see Eq.(20)). Other parameters as in Fig.6.

FIGURE 8:
Extended Hubbard inverse photoemission ($! < E_F$) and photoemission ($! > E_F$) hole spectral densities for different hole dopings x . The vertical line indicates the position of the Fermi level E_F . Parameters are given by the set 1 of table II.

FIGURE 9:
Same as Fig.8 for the set 3 of table II.

FIGURE 10:
Total amount of occupied hole states in the upper band W minus two times the hole doping x , as a function of x for the three sets of parameters of Table I and II. For $U \neq 1, W - 2x = 0$.

FIGURE 11:
Dressed weight and average kinetic energy of the effective model Eq.(5) as a function of doping. Parameters are given by the set 3 of table II.

FIGURE 12:
Optical conductivity for different doping levels and the set 3 of parameters of table II. The delta function contribution at $! = 0$ has been replaced by a Lorentzian of width 0.01 to facilitate the comparison with experiment.

FIGURE 13:
Same as Fig.12 for the set 2.

FIGURE 14:
Bottom : spectral densities of $\text{Im} \text{ag} \langle \langle j_i j_j \rangle \rangle$ (contributions to the optical conductivity) of the partial currents $j_{AB}; j_{BA}$ and the total result (see Eqs.(10) and (13)) for $x = 0.2$ and the set 2 of parameters of Table II. Top: corresponding hole spectral density. The arrows indicate the transitions which give rise to the different contributions to the optical conductivity.

FIGURE 15:
Effective number of carriers defined by Eq.(21) as a function of frequency for different doping levels and the sets of parameters 3 and 2 of Table II.

TABLES

TABLE I: Different sets of parameters of the three-band Hubbard model H_{3b} (Eq.1) in units of t_{pd} .

| Set | U_d | U_{pd} | t_{pp} | U_p |
|-----|-------|----------|----------|-------|
| 1 | 2.0 | 7 | 1 | 0.5 |
| 2 | 2.5 | 9 | 1 | 0.5 |
| 3 | 4.0 | 7 | 1 | 0.5 |

TABLE II: Effective one-band parameters for the three sets of parameters of H_{3b} listed in Table I. The last column gives the ratio of the effective on-site repulsion U to the average effective hopping $t_m = (t_{AA} + 2t_{AB} + t_{BB})/4$.

| Set | U | t_{AA} | t_{AB} | t_{BB} | V_{11} | V_{12} | V_{22} | $U=t_m$ |
|-----|------|----------|----------|----------|----------|----------|----------|---------|
| 1 | 2.15 | 0.382 | 0.385 | 0.337 | 0.123 | 0.170 | 0.178 | 5.78 |
| 2 | 3.01 | 0.377 | 0.324 | 0.338 | 0.119 | 0.162 | 0.181 | 8.85 |
| 3 | 3.37 | 0.268 | 0.327 | 0.337 | 0.066 | 0.125 | 0.156 | 10.71 |

TABLE III: Exact gap E_g compared with the gap E_g^{av} obtained after averaging over boundary conditions and E_g^f for fixed (antiperiodic) boundary condition for a ring of 8 sites and different values of $U=t$.

| $U=t$ | E_g | $E_g^{av}(8)$ | $E_g^f(8)$ |
|-------|--------|---------------|------------|
| 4 | 1.2868 | 1.98 | 3.68 |
| 6 | 2.8928 | 3.50 | 4.90 |
| 8 | 4.6796 | 5.21 | 6.47 |

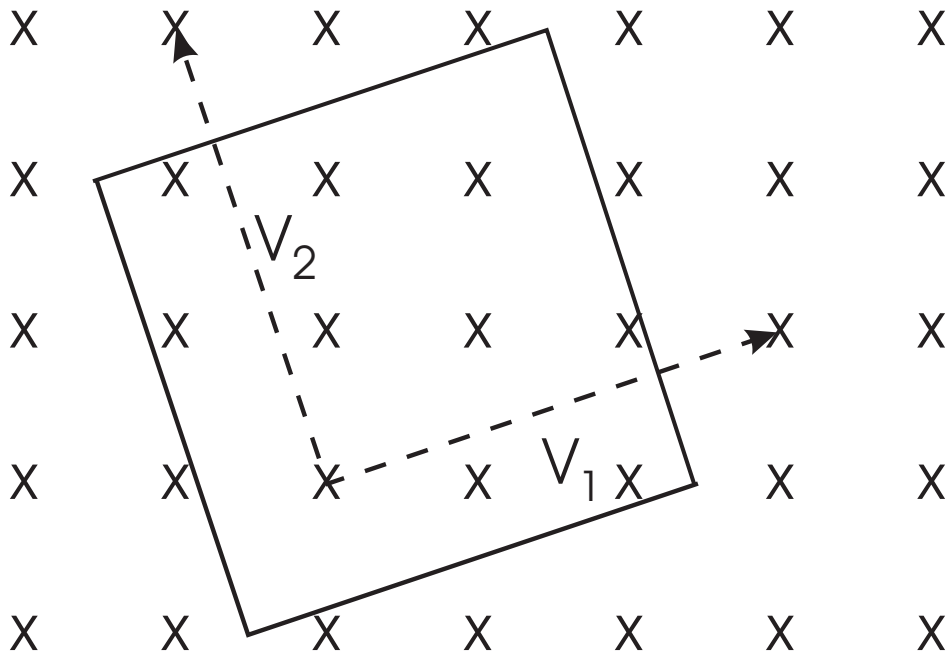
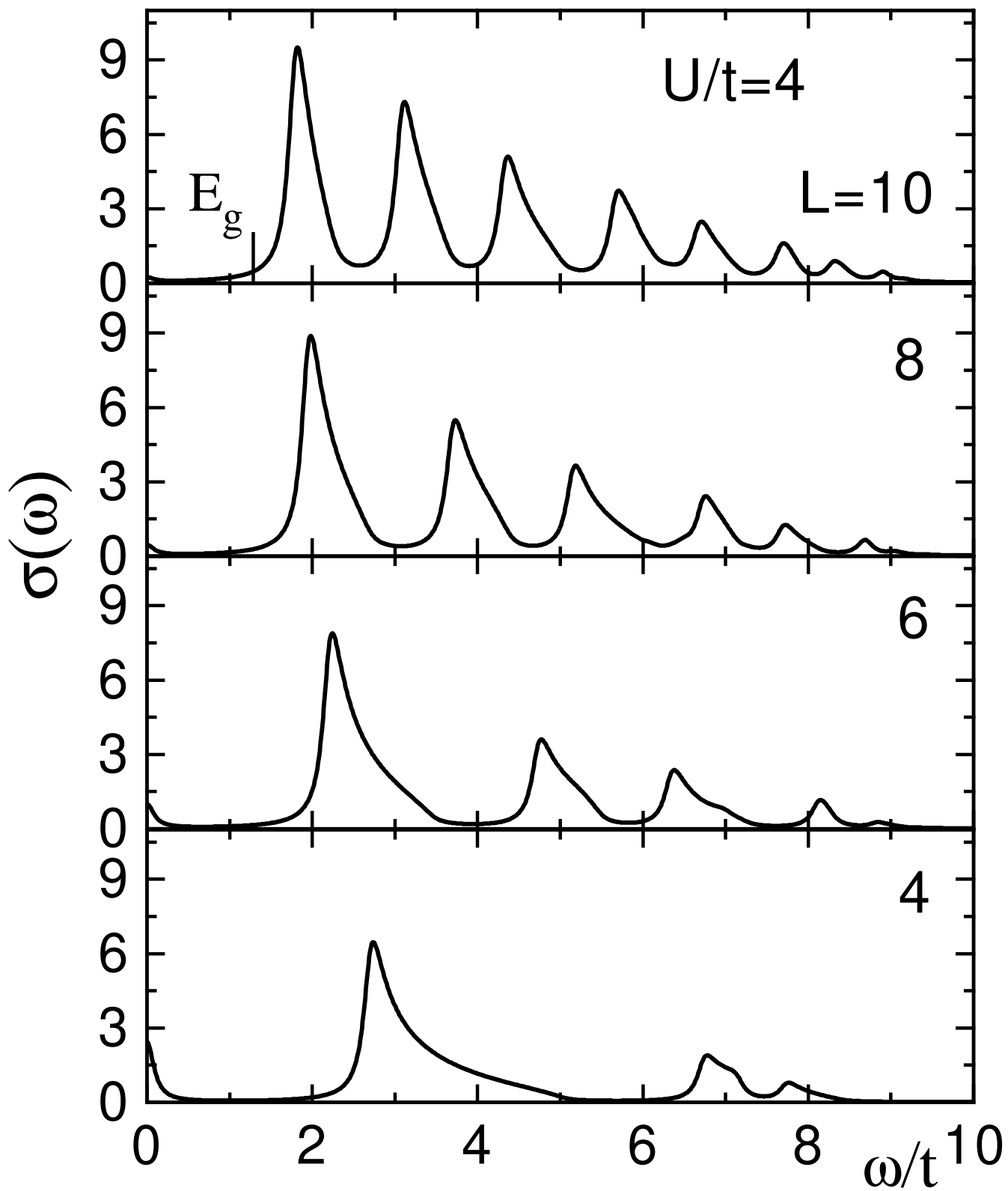
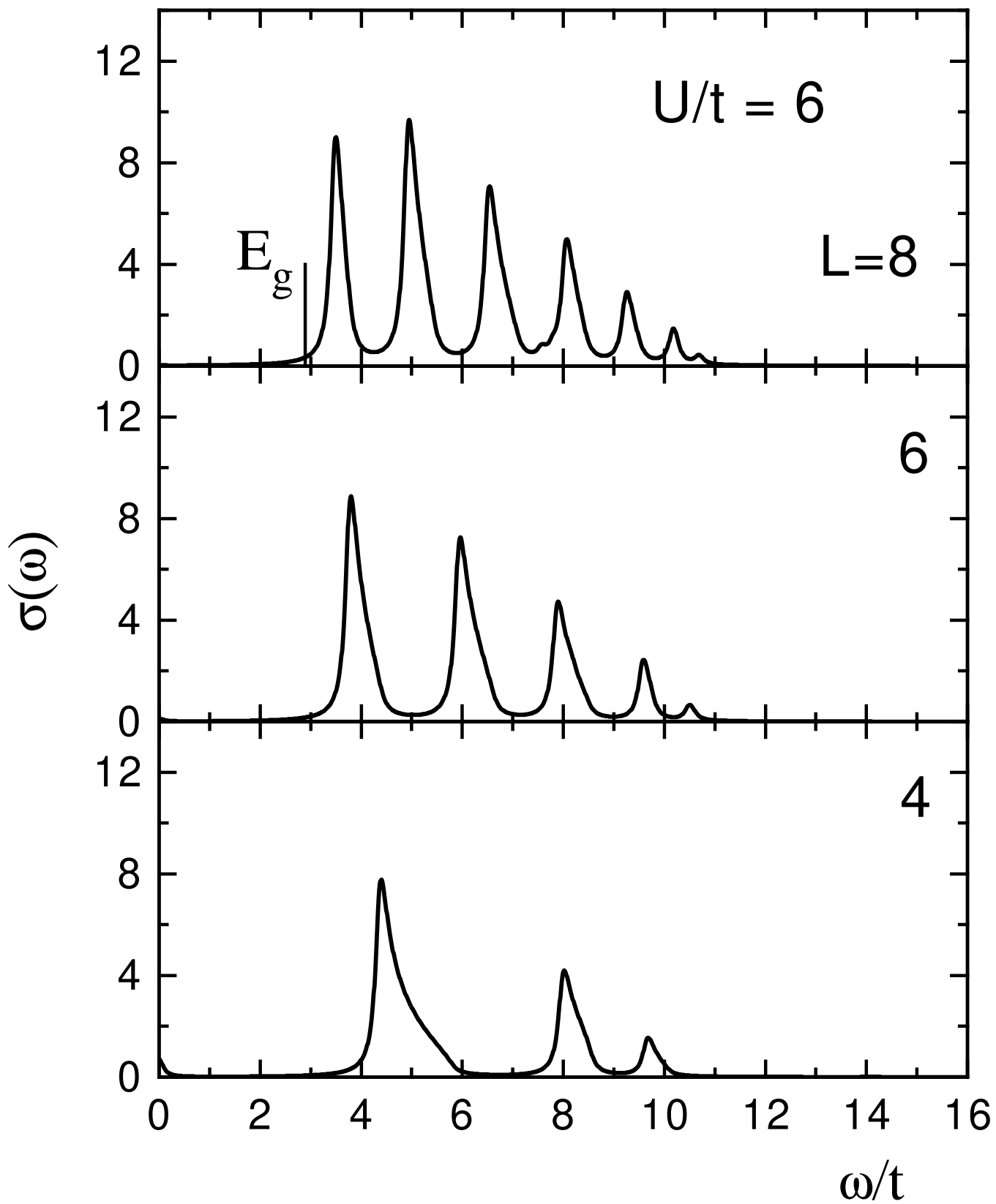


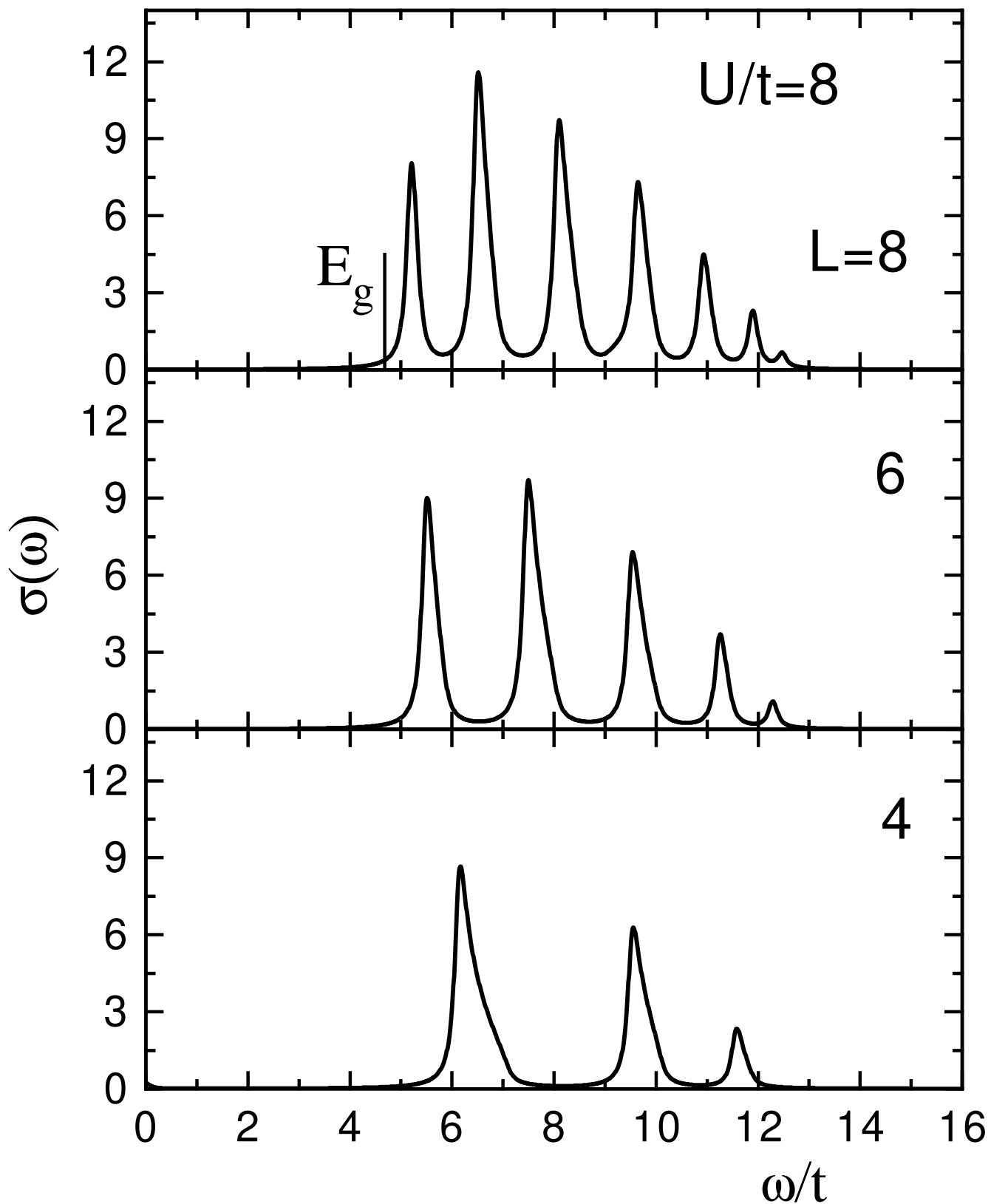
Fig.1 Simon et. al.



Simon et al.Fig.2

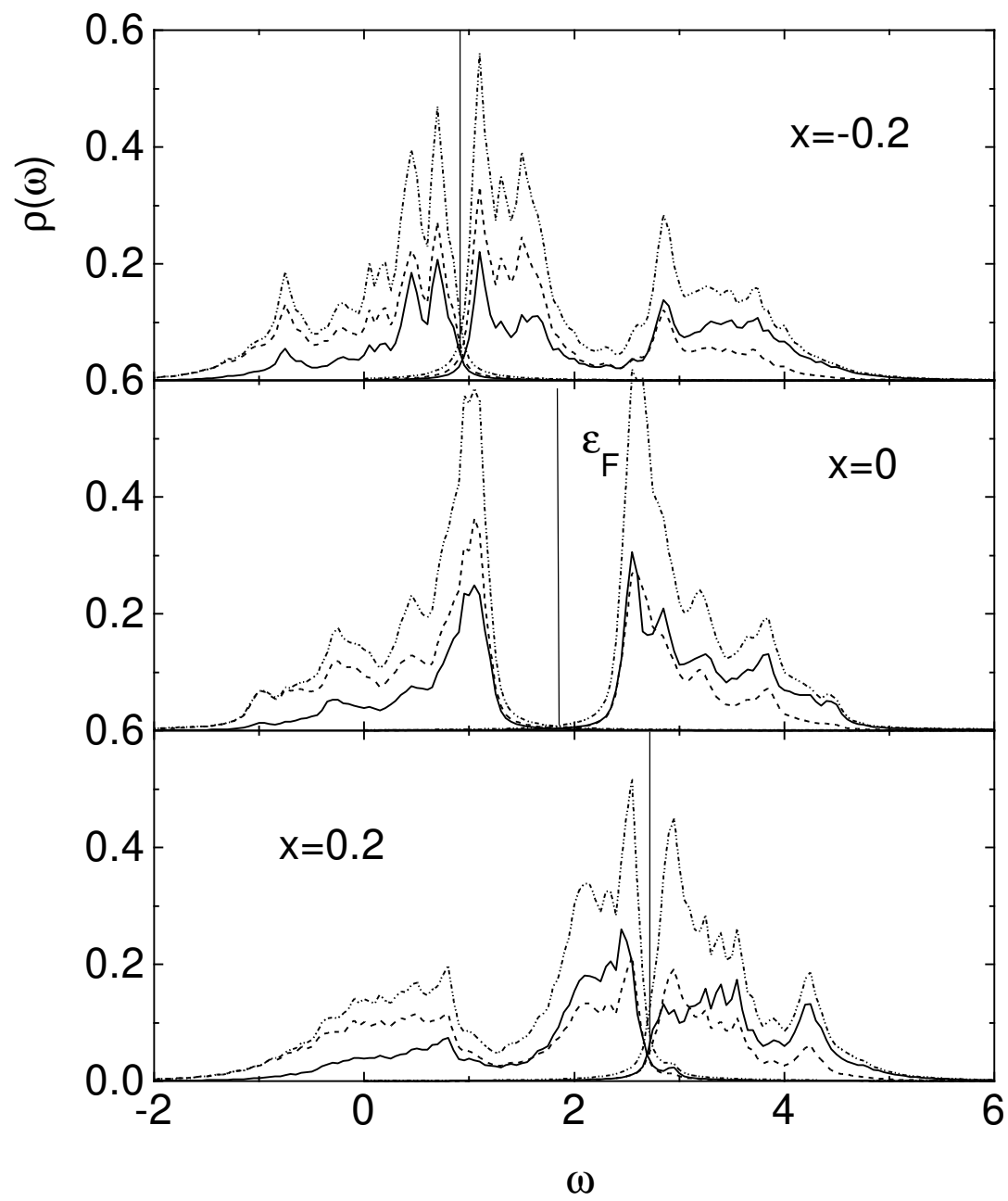


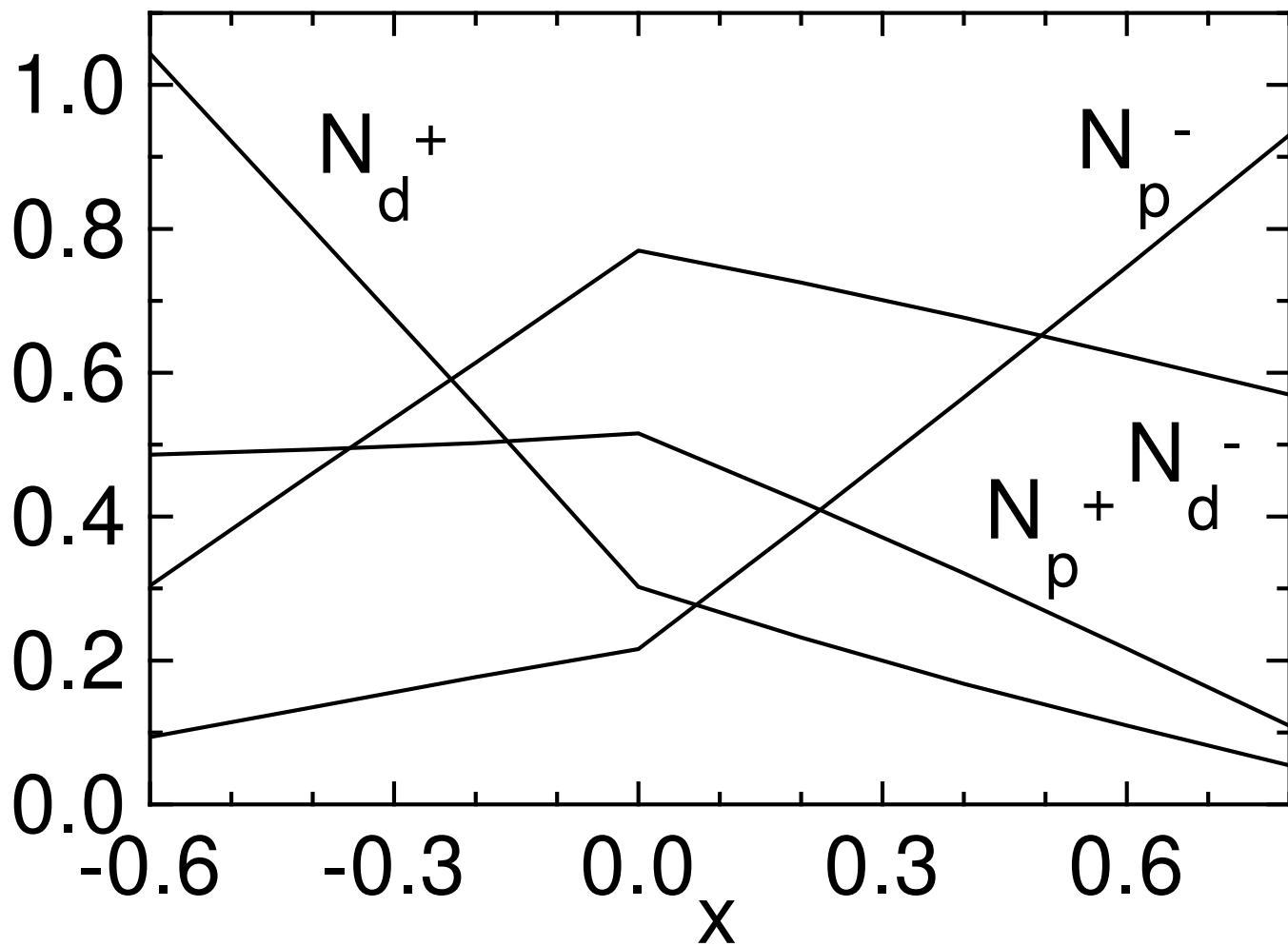
Simon et al. Fig. 3



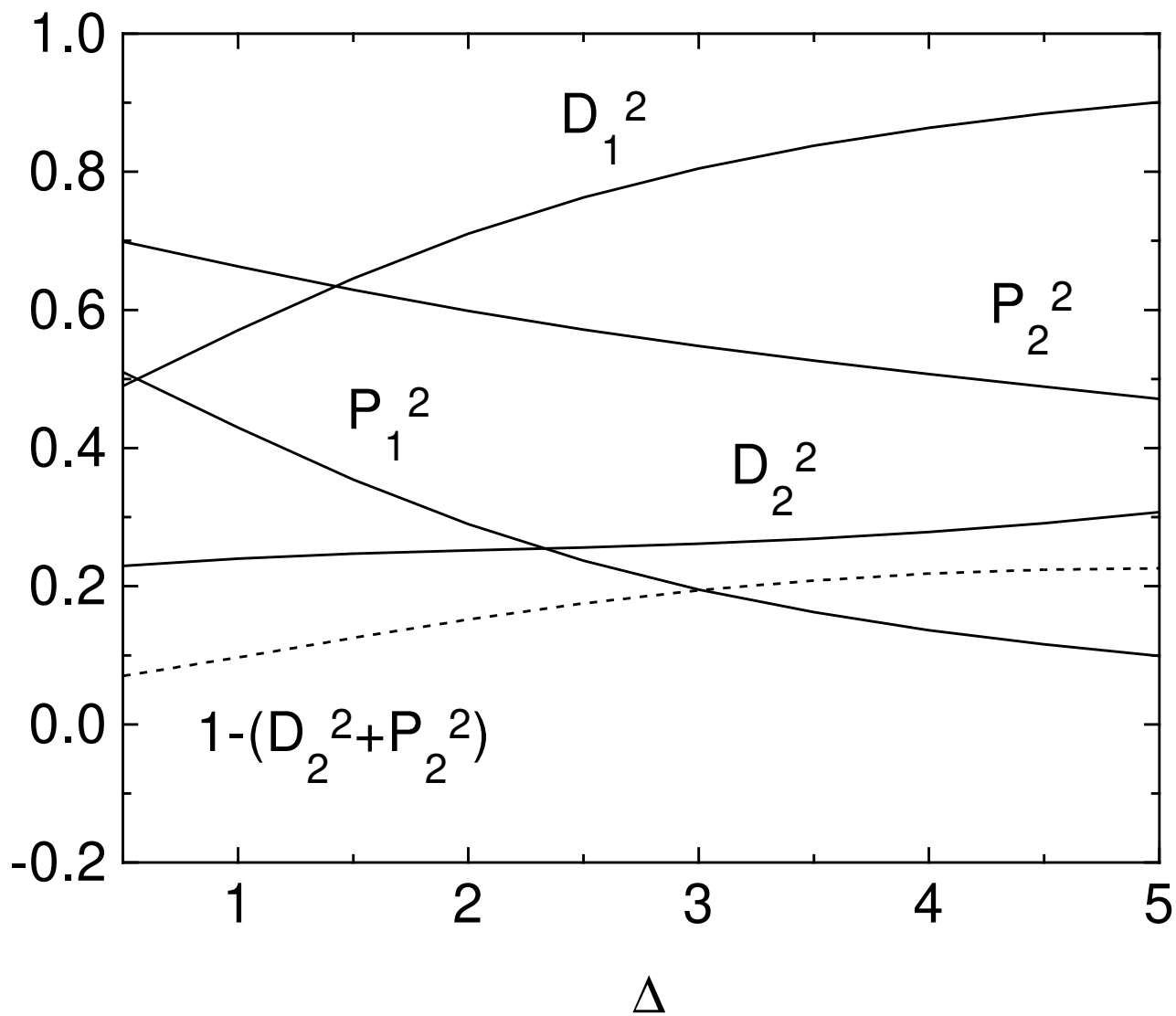
Simon et al. Fig. 4

Fig. 5 Simon et. al.





Simon et. al Fig. 6



Simon et. al. Fig. 7

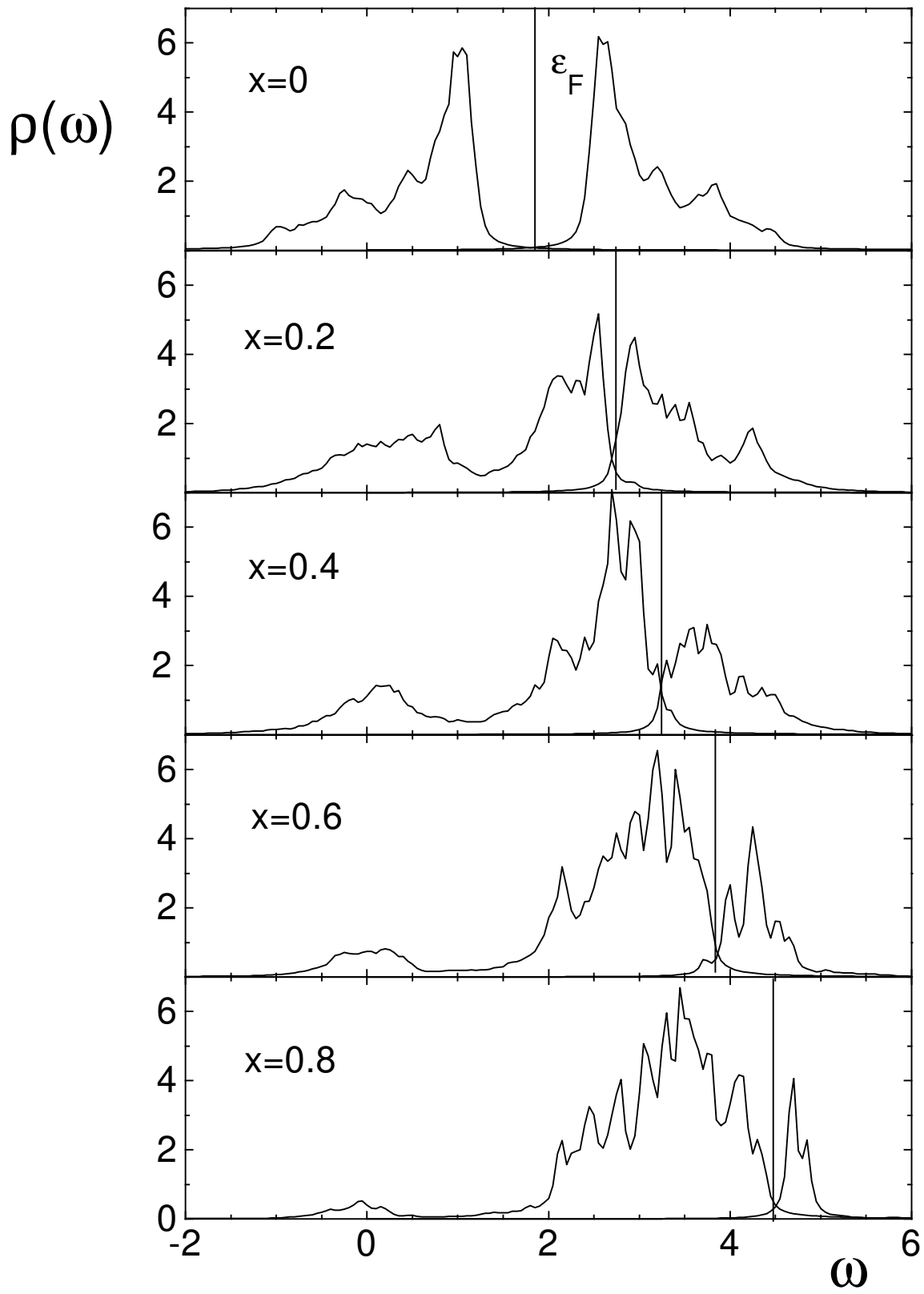


Fig. 8 Simon et. al.

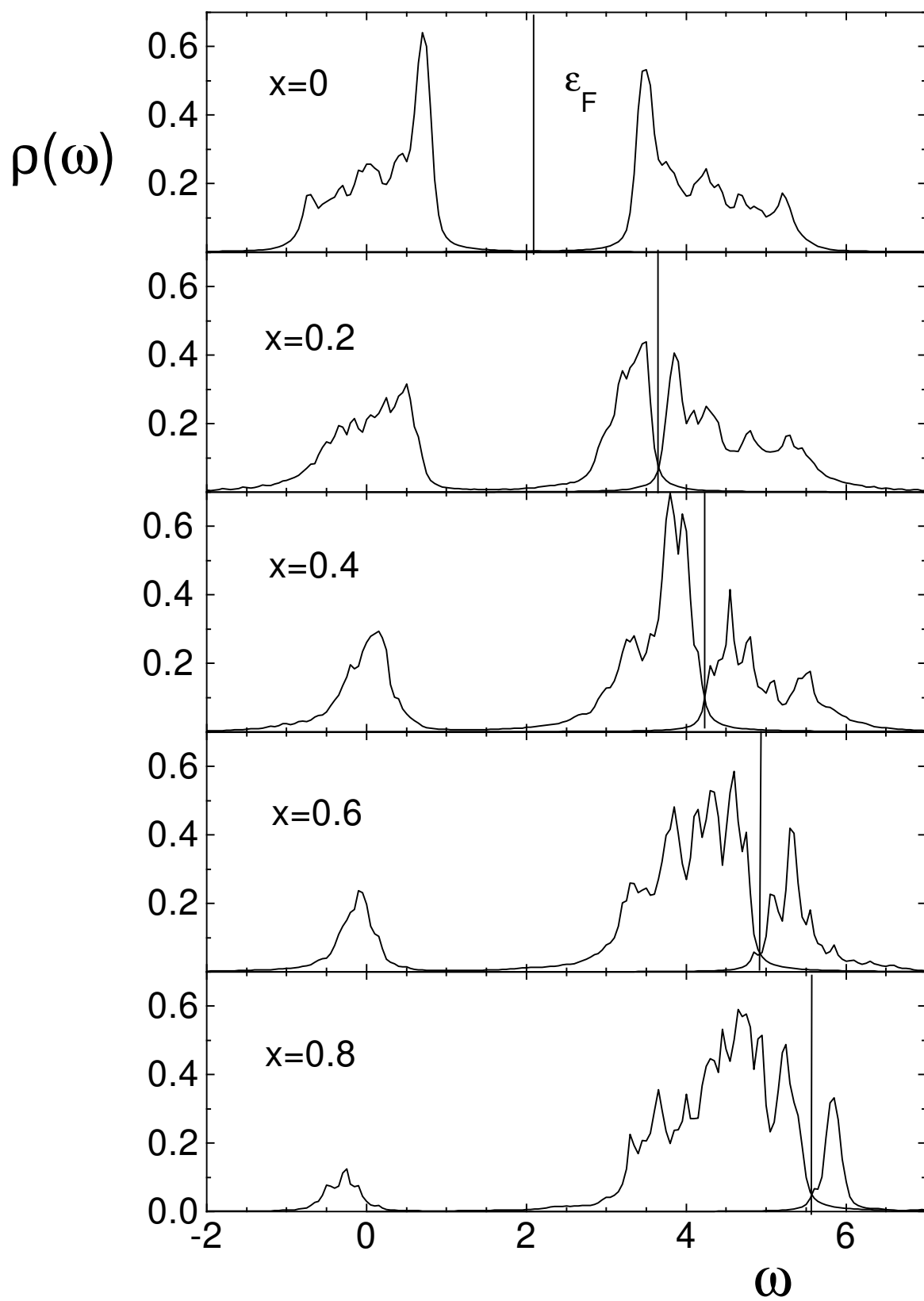


Fig. 9 Simon et. al.

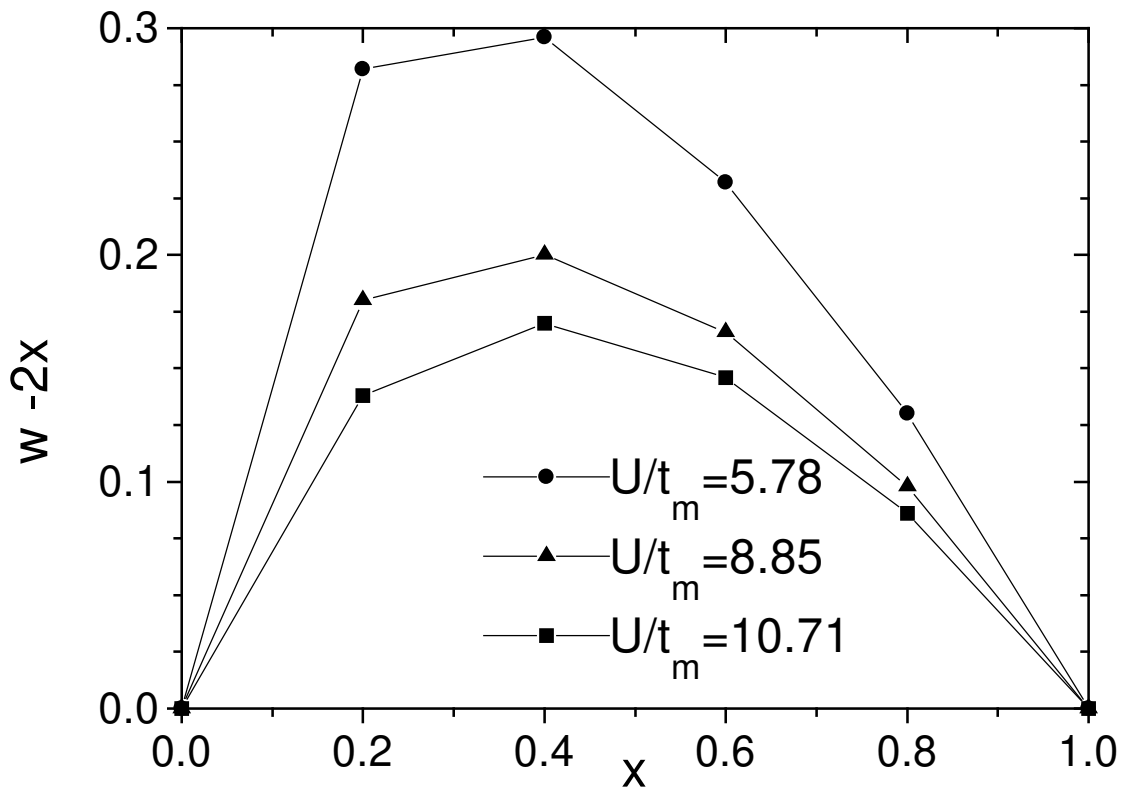


Fig. 10 Simon et. al.

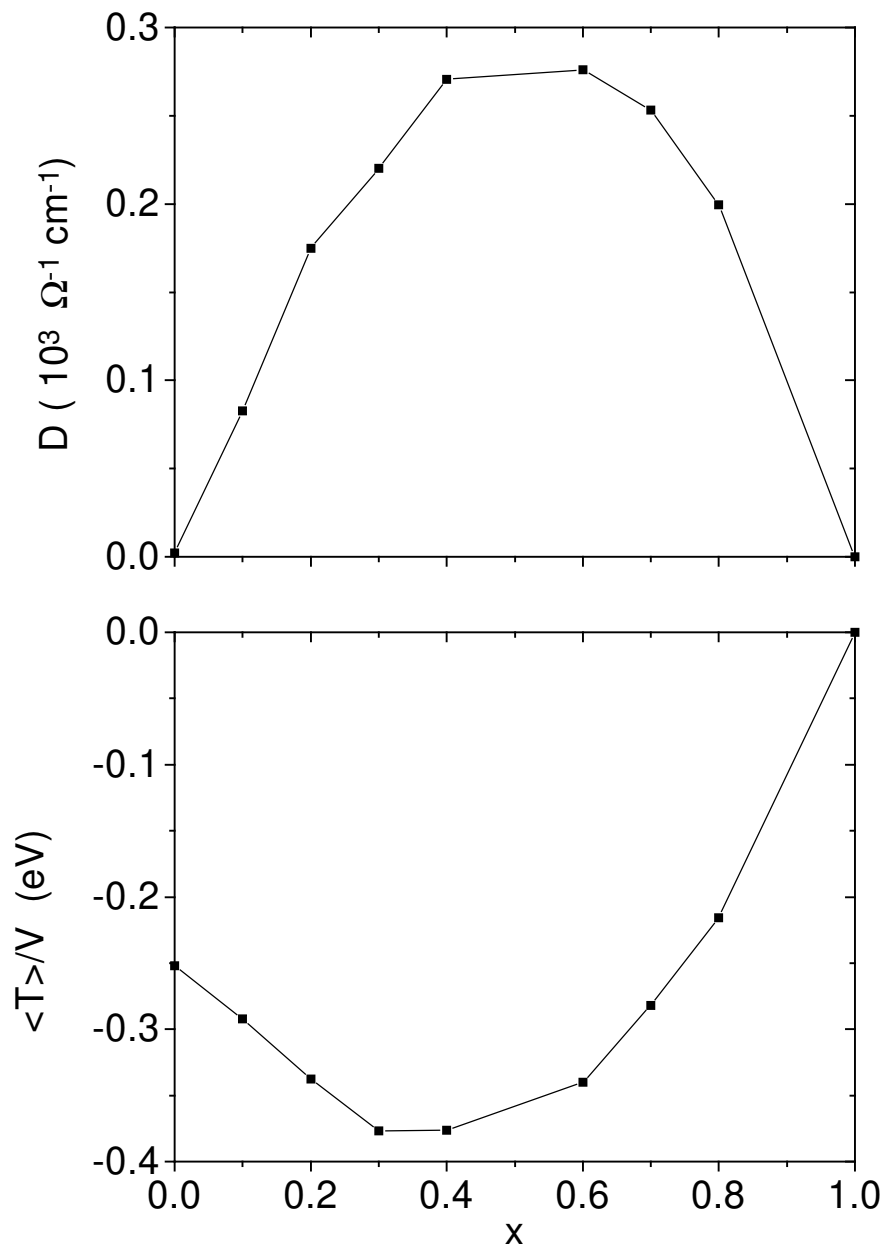


Fig. 11 Simon et. al.

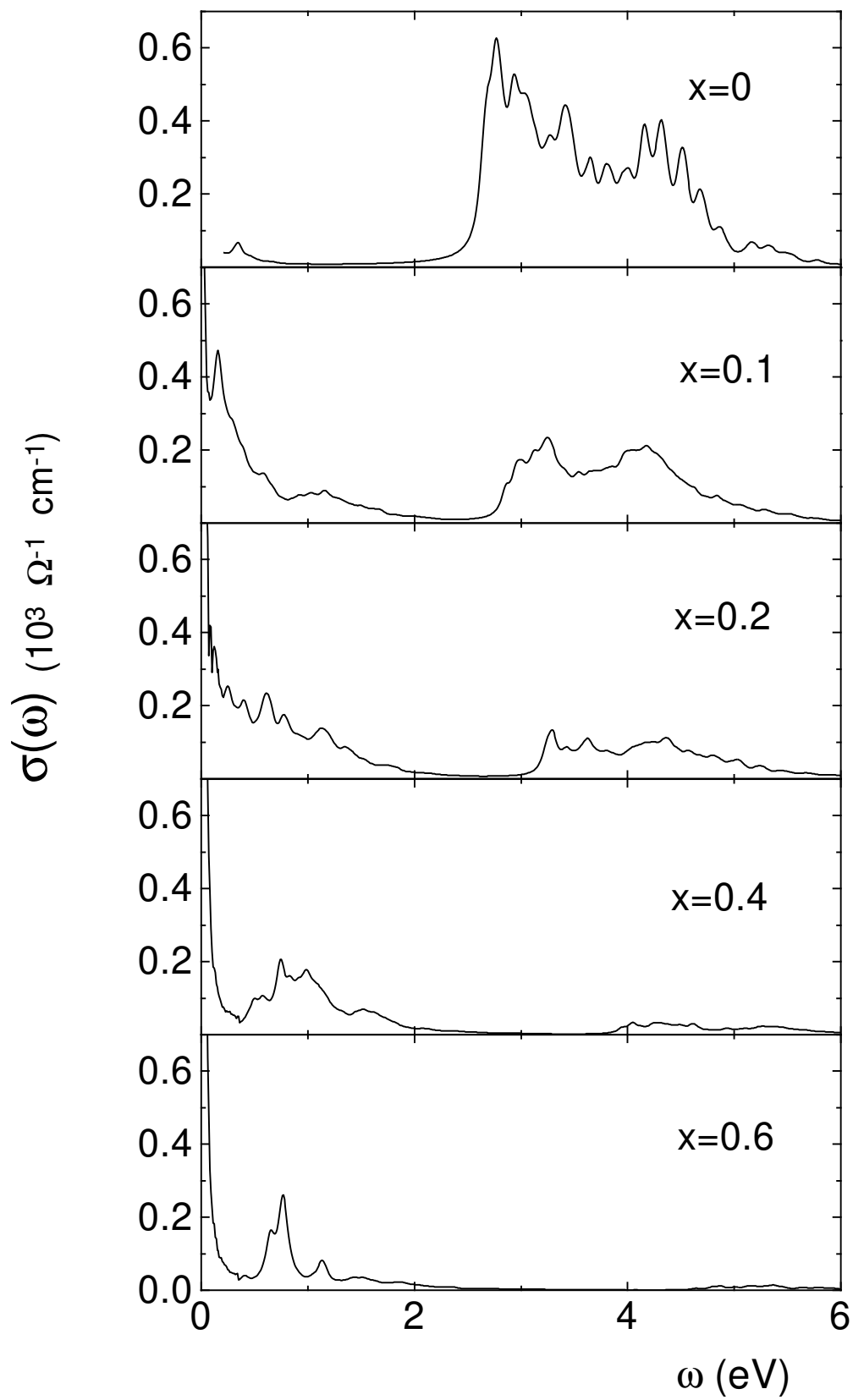


Fig. 12 Simon et. al.

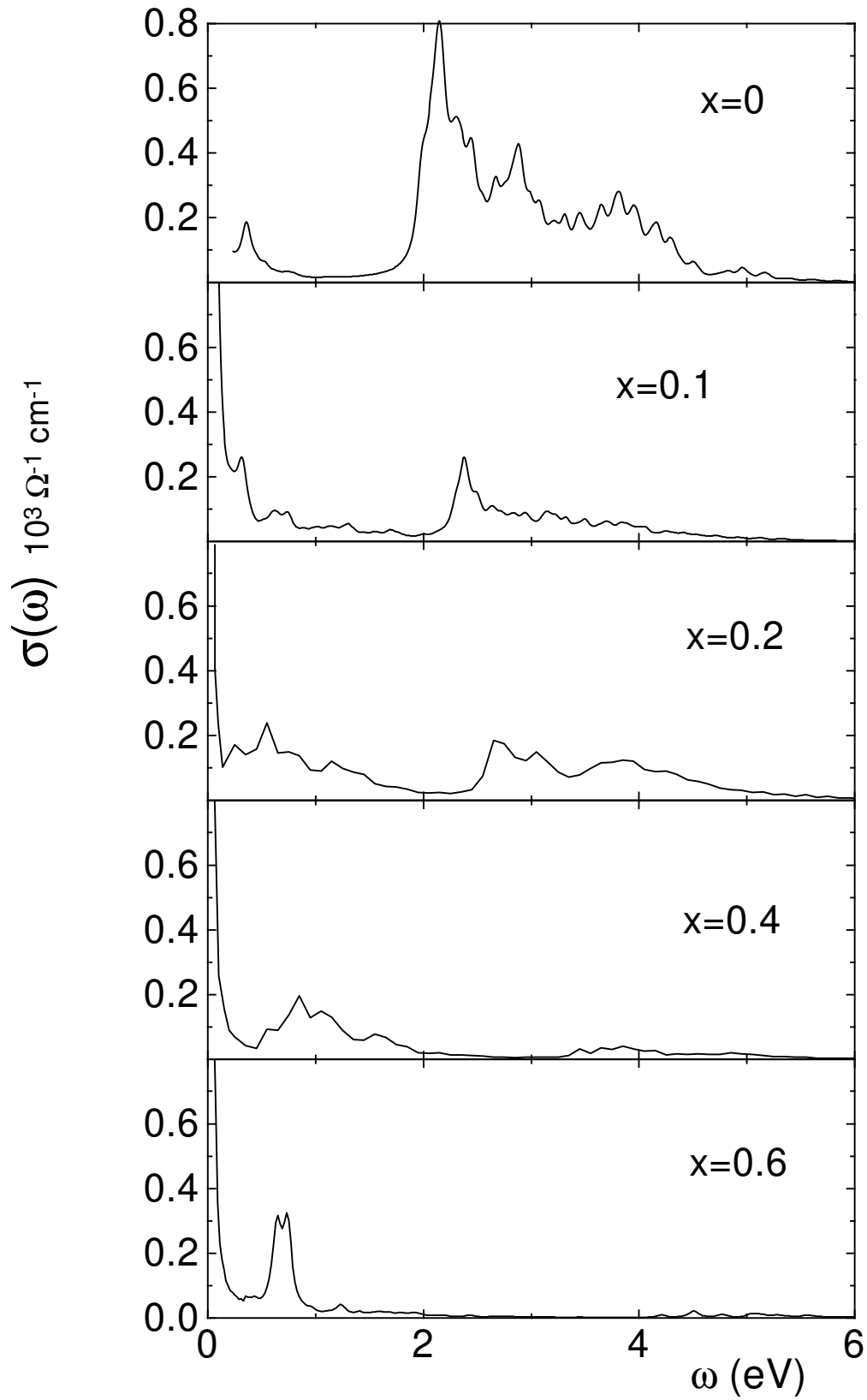


Fig. 13 Simon et. al.

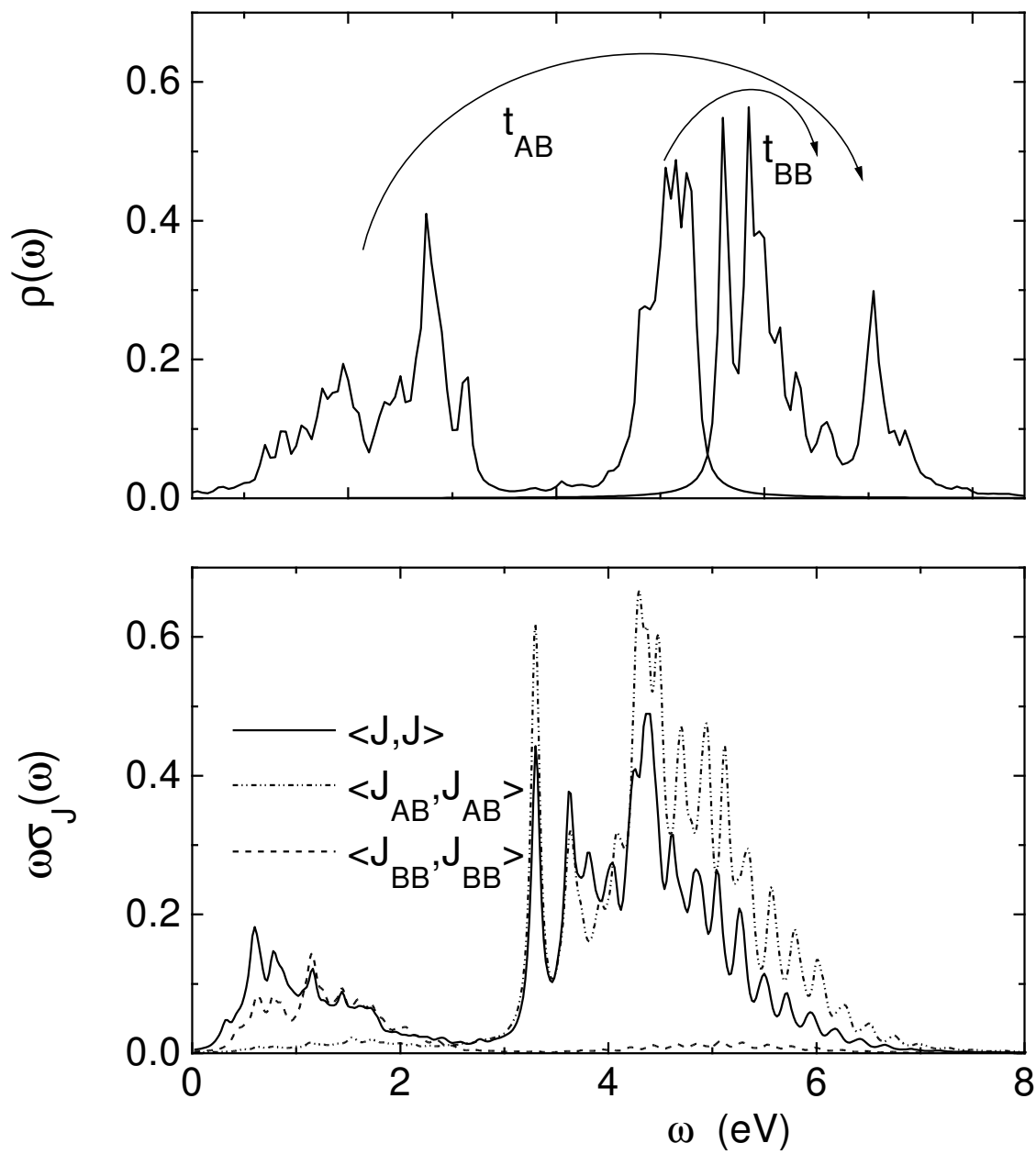


Fig. 14 Simon et. al.

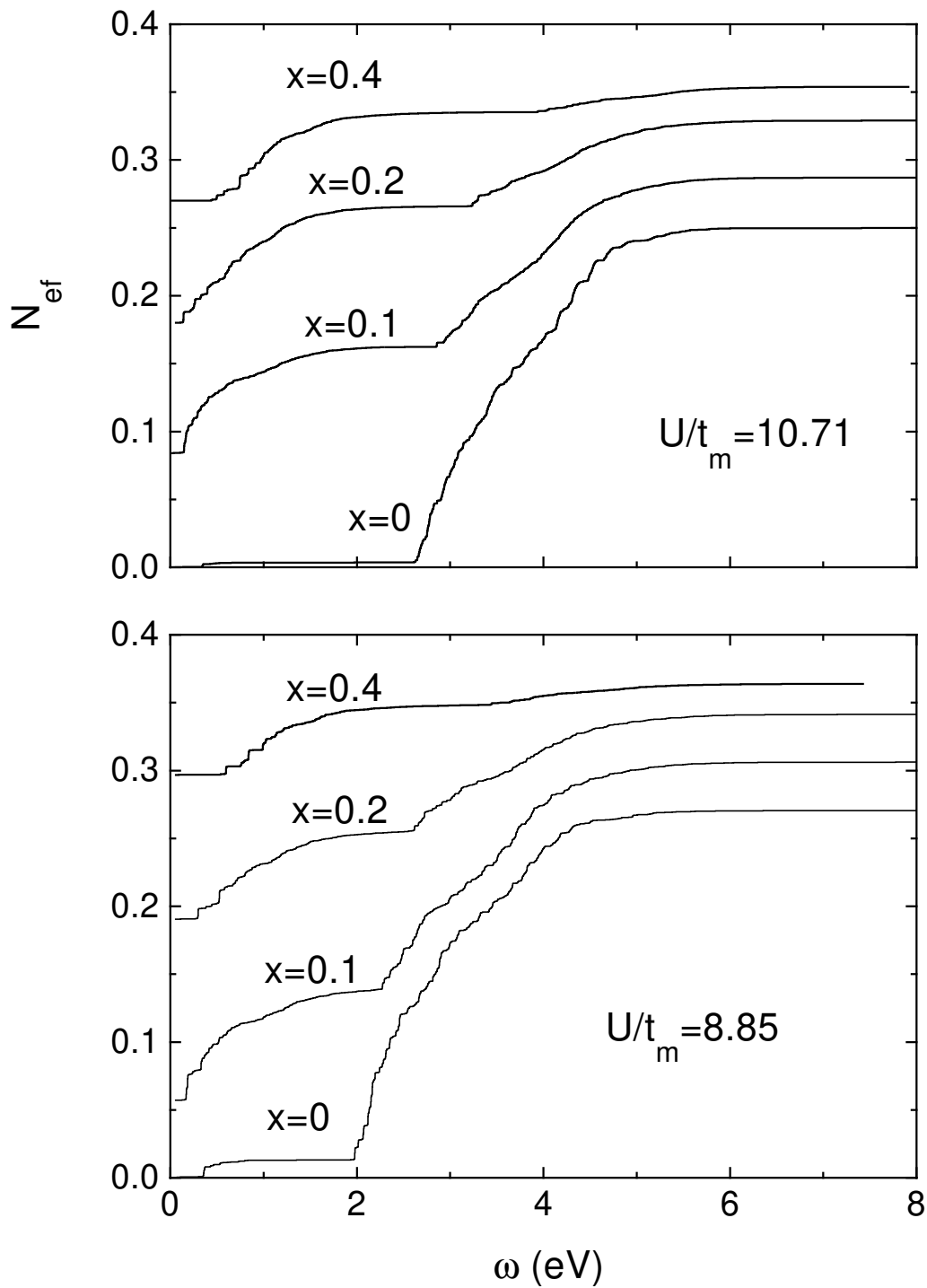


Fig. 15 Simon et. al.

